ARTICLE

Predicting Polymer Nanofiber Interactions via Molecular Simulations

Sezen Buell,[†] Gregory C. Rutledge,[‡] and Krystyn J. Van Vliet*[,†]

Department of Materials Science and Engineering and Department of Chemical Engineering, Massachusetts Institute of Technology, Cambridge, Massachusetts 02139

ABSTRACT Physical and functional properties of nonwoven textiles and other fiberlike materials depend strongly on the number and type of fiber−fiber interactions. For nanoscale polymeric fibers in particular, these interactions are governed by the surfaces of and contacts between fibers. We employ both molecular dynamics (MD) simulations at a temperature below the glass transition temperature T_g of the polymer bulk, and molecular statics (MS), or energy minimization, to study the interfiber interactions between prototypical polymeric fibers of 4.6 nm diameter, comprising multiple macromolecular chains each of 100 carbon atoms per chain (C100). Our MD simulations show that fibers aligned parallel and within 9 nm of one another experience a significant force of attraction. These fibers tend toward coalescence on a very short time scale, even below T_g. In contrast, our MS calculations suggest an interfiber interaction that transitions from an attractive to a repulsive force at a separation distance of 6 nm. The results of either approach can be used to obtain a quantitative, closed-form relation describing fiber−fiber interaction energies $U(s)$. However, the predicted form of interaction is quite different for the two approaches, and can be understood in terms of differences in the extent of molecular mobility within and between fibers for these different modeling perspectives. The results of these molecular-scale calculations of $U(s)$ are used to interpret experimental observations for electrospun polymer nanofiber mats. These findings highlight the role of temperature and kinetically accessible molecular configurations in predicting interface-dominated interactions at polymer fiber surfaces, and prompt further experiments and simulations to confirm these effects in the properties of nonwoven mats comprising such nanoscale fibers.

KEYWORDS: polymer nanofibers • electrospinning • interaction potential • molecular simulation

INTRODUCTION

Nonwoven materials comprising continuous polymer fibers can be fabricated via several approaches, such as electrospinning, with fiber diameters ranging from micrometers to tens of nanometers. Such nonwoven fiber mats and meshes have been advocated for use in filters, composites, fuel cells, personal protection, catalyst supports, drug delivery devices, tissue scaffolds, and other applications (1−5). Of fundamental necessity for many of these applications is an understanding of the mechanical performance of these nonwoven materials, which is determined by the nanofiber volume fraction and orientation distribution, the mechanical properties of individual nanofibers, and the interactions among adjacent nanofibers. As electrospun nonwoven materials exhibit a particularly high number of fiber−fiber junctions, this interfiber interaction is especially important in determining the macroscopic mechanical properties of such mats. For example, it has been shown that interfiber bonding can be enhanced by controlling the electrospinning process (6) or by post-spinning treatments (7−10), and that this enhancement can improve macroscopic tensile strength and failure strain considerably (8). Choi et al. showed that the thermal treatment of electrospun poly(etherimide) (PEI) fiber mats leads to interfiber bonding and improved tensile strength (10). Similarly, the presence of residual solvent in the electrospun polymeric nanofibers may facilitate adhesion between nanofibers in contact, and thereby change the mechanical properties of the mat (11−13). Kidoaki et al. showed that the Young's elastic modulus of segmented polyurethane (SPU) meshes increased with increasing *N*,*N*-dimethylformamide (DMF) content, when electrospun from a mixed solvent system of tetrahydrofuran (THF) and DMF (13). These authors attributed the increased mesh stiffness to a higher degree of interfiber bonding, reasoning that the residual content of the slower-evaporating DMF may facilitate entanglement of chains from different fibers at contact points.

One of the challenges in the macroscopic modeling of nonwoven materials is the accurate representation of the fiber−fiber contact interactions. Since the 1950s, several models have been developed, each based on various assumptions of fiber−fiber contact configurations and deformation mechanisms (14−19). For example, Pan et al. included the effect of interfiber friction and sliding on the mechanical response of fiber assemblies and modeled the compression hysteresis behavior of these assemblies. This model was found to be in reasonable agreement with uniaxial compression experiments of textile treatment wool (14). Wang et al. showed that simple Euler−Bernoulli beam elements connected by torsion springs at the fiber−fiber junctions can represent the mechanical properties of fibrous networks successfully (17). In one effective medium model, the

* Corresponding author. E-mail: krystyn@mit.edu.
Received for review January 6, 2010 and accepted March 26, 2010
† Department of Materials Science and Engineering, Massachusetts Institute of Technology.
‡ Department of Chemical Engineering, Massachusetts Institute of Technology.
DOI: 10.1021/am1000135

Published on Web 04/12/2010

fibers were assumed to be rigidly bonded at each fiber−fiber crossing (18); in this model, when the network is deformed, the angles between crossing fibers remain constant, and elastic strain is borne entirely in the fiber segments between the crossings. The application of this theory to two-dimensional (2D) random fiber networks was found to agree well with results from numerical simulations (18). In another study, Wu et al. represented a planar fiber network via a micromechanical model in which the linearly elastic straight rods were bonded rigidly at fiber−fiber contacts (19). The authors compared the model predictions at several fiber volume fractions with finite element analysis, and found the two to be in good agreement. Chatterjee introduced an energy penalty for rupturing an existing fiber−fiber contact, to calculate the tensile and shear elastic moduli of three-dimensional fiber networks (20). He estimated the strains at the elastic limits under tensile and shear deformation, but did not compare those results with experiments.

Although these models generally compared favorably against available experiments and/or numerical simulations, the constraints on the fiber−fiber junction interactions were assumed without confirmation by direct experimental measurements or finer-scale simulations. Direct experimental measurements of fiber−fiber interactions are very challenging, particularly for polymeric fibers of submicrometer diameter, because of the difficulty of isolating and handling fiber−fiber couples and the uncertainties involved in measuring forces and energies at this scale. Such experimental challenges are not unique to electrospun fiber networks, but arise also in a broad range of mechanically compliant fibers and nonwoven materials, including the proteinaceous filament networks comprising extracellular matrices and intracellular cytoskeletons. To the best of our knowledge, direct experimental measurements of such interactions for electrospun materials have not been reported previously. At the continuum scale, theoretical calculations for the surface adhesion of two cylindrical elastic bodies as a function of geometry (diameter and mutual orientation) and properties (surface energy and elastic modulus) have been reported by Wu and Dzenis (21). Here we report a molecular simulation-based analysis of interfiber interactions among nanoscale polymeric fibers, in order to develop a fiber−fiber interaction model that can be employed in network calculations. In the next section, we describe our model and simulation techniques. We then report the results of two different approaches to study interfiber interactions as a function of separation distance, based on molecular dynamics (MD) and molecular statics (MS), respectively. Finally, we compare these results and molecular-scale modeling perspectives with continuum-scale analytical predictions and discuss the conditions under which the results from these two different types of simulations can be applied to describe interfiber interactions.

SIMULATION METHODS

To create polymeric fibers of nanoscale diameter with atomistic detail, we first employed MD simulations using a large scale atomic/molecular massively parallel simulator (LAMMPS) (22). The united atom (UA) force field used in these simulations combines the hydrogen atoms with the carbon to which they are attached into a single "bead"; this model was parametrized by Paul et al. (23) for polyethylene (PE), and later modified by Bolton et al. (24) and In't Veld et al. (25). This is the same force field that we have used previously to characterize the structural, thermal (26), and mechanical (27) properties of individual nanofibers. The details of the functional form and parameters can be found elsewhere (26, 27).

A single, free-standing nanofiber was prepared using a two-step MD method as we have described previously (26, 27). First, a cubic simulation box containing 30 chains of 100 UA beads (designated C100) was created (total number of monomers $N = 3000$) and equilibrated in the NVT ensemble at 495 K, such that the polymer density was 0.75 g/cm^3. Then the simulation box was cooled to 100 K through a succession of NPT ensembles with a constant, isotropic pressure of $P = 1 \times 10^5$ Pa. This temperature is lower than both the glass transition temperature (T_g) of the same material (united atom C100, or 100 carbon atoms per chain of UA PE) in the bulk state, which has been estimated to be 280 K (28), and the T_g of the surface layer of a single C100 nanofiber, which we have previously estimated to be 150 K (26). Next, the box dimensions were increased simultaneously in two perpendicular directions (i.e., x and y), such that the macromolecules can no longer interact with their images in these directions. Thus, the periodic boundary condition applied only in one direction, the z-direction, which was then parallel by definition to the fiber axis. This simulation cell was then equilibrated in an NVT ensemble at 100 K, resulting in spontaneous formation of a cylindrically symmetric object and representing a repeating segment of an amorphous nanofiber of infinite length. The growth of Rayleigh instabilities was suppressed by choosing the simulation box length to be sufficiently short, such that $L_z < 2\pi R_{fiber}$ (26).The radius of the nanofiber thus created was calculated to be $R_{fiber} = 2.3$ nm, using the Gibbs dividing surface (GDS) method as described previously (26). For the purposes of this study, a single-fiber radius was considered so that multiple simulation approaches and parameters could be compared systematically.

Two distinct approaches, MD and MS (which is also called "energy minimization"), were then considered to construct interfiber interaction energy functionals $U(s)$ over a range of separation distances s. For both simulation approaches, the total potential energy of the system was calculated by addition of bond, angle, torsional and Lennard-Jones energies between united atoms. Note that here we reserve U for interaction energy and E for total potential energy. The interfiber separation distances considered were in the range $1 \text{ nm} < s < 11$ nm, thereby intentionally considering interaction energies for initial conditions of significant fiber−fiber overlap (for $s < 2R_{fiber} \approx 4.6$ nm).

To characterize interfiber interactions via MD, we constructed a system comprising two C100 nanofibers, each prepared as described above and then placed in the same simulation box such that the axes of the fibers were parallel and separated by a prescribed distance s (Figure 1a). Here $s = s(r_1^{3N}, r_2^{3N})$ is defined by the distance between the centers of mass (COM) of the two fibers, which in turn are computed from the 3N coordinates of the united atoms initially assigned to each fiber; we considered ten different interfiber distances over the range $1 \text{ nm} < s < 11$ nm. Figure 1b shows the initial configuration of the simulated system at a separation distance $s = 7$ nm. Figure 1c illustrates that R_{fiber} is rigorously defined in terms of mass density, but is less than the distance of maximum chain extension from the fiber center; in other words, portions of chains extend further than R_{fiber} and give rise to interfiber interactions at $s > 2R_{fiber}$. To maintain each interfiber distance constant, we fixed the momentum of the COM of each nanofiber to zero via the "fix momentum" command in LAMMPS.

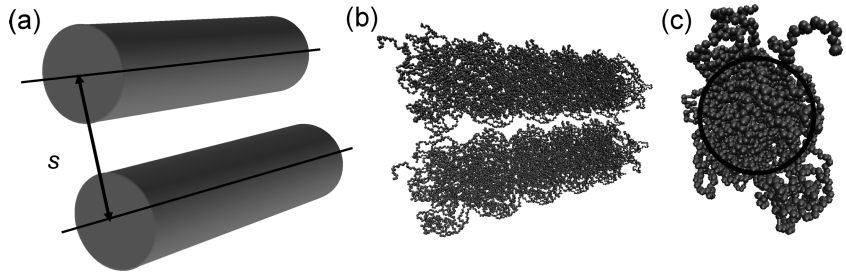

FIGURE 1. (a) Schematic representation of the fiber−fiber simulations system. (b) Visual Molecular Dynamics (VMD) image of the fiber−fiber simulation setup at interfiber distance $s = 7$ nm. Five periodic images in the axial direction are connected for clarity ($R_{fiber} = 2.3$ nm at 100 K). (c) Cross-section of one fiber, indicating both the fiber radius, as defined by the Gibbs dividing surface method (26), and the instantaneous position of UA beads. It is clear that portions of the polymer chains extend beyond the distance $R_{fiber} = 2.3$ nm from the fiber center.

Although this method does not affect the relative motion of the atoms within either nanofiber, it ensures that the COMs of the two nanofibers remain at the initial separation distance throughout the entire simulation duration. (Again, significant overlap between fibers was expected for $s < 2R_{fiber} \approx 4.6$ nm. Thus, for interfiber distances $s < 5$ nm, calculations of energy via extended MD simulations over 100s ns were preceded by a brief energy minimization for 100 steps to eliminate any energetically prohibited overlaps between initial atomic positions, as dictated by the interatomic potential of the UA polyethylene model.) The system was then equilibrated in the NVT ensemble at 100K for 300 ns. These MD simulations thus provide estimates of $E(t)$, $E(s)$, and $U_{MD}(s)$ for conditions under which thermally activated motion is sampled over sufficient time to permit reconfiguration of chains within and between fibers.

In addition, we also performed MS or energy minimization numerical calculations of the same fiber-pair system, with the same constraint on separation distance s. The purpose of the interfiber MS calculations was to determine $U_{MS}(s)$ in a manner that, in contrast to MD, precludes any significant or thermally activated reorganization of the macromolecules within the constituent fibers. The same two-fiber simulation box setup was used as in the MD interfiber simulations, with nanofibers positioned parallel to the long axis at an interfiber distance that ranged 1 nm $< s <$ 11 nm. The energy minimization algorithm iteratively adjusted atomic coordinates to lower the system energy, and iterations were terminated when the configuration attained a local potential energy minimum with tolerance within 0.01 J/mol UA. To sample more two-fiber systems and thus obtain better statistics on calculated energies, we generated several initial configurations of fiber pairs by rotating one of the fibers about its z-axis by 10° increments.

RESULTS AND DISCUSSION

Below we discuss two different interaction potentials. The first is obtained under conditions of thermal motion as represented by the MD simulations, and the second is obtained from the static configurations obtained by MS calculations.

Interfiber Interaction Potential Constructed from MD Simulations. *Potential Energy Profiles.* From the MD simulation results, the total potential energy E(s) of the fiber-pair systems was used to calculate the interaction energy U(s) between the nanofibers as a function of fiber COM separation distance s. Figures 2a and 2b show the change in total potential energy as a function of time $E(t)$ for the MD simulations at $s = 2$, 5, 7, and 9 nm. Potential energy profiles at $s = 3$, 4, 6, and 8 nm follow trends similar to those shown in Figure 2a, and are omitted for clarity. Potential energy profiles at $s = 10$ nm superpose the data obtained at $s = 9$ nm in Figure 2b.

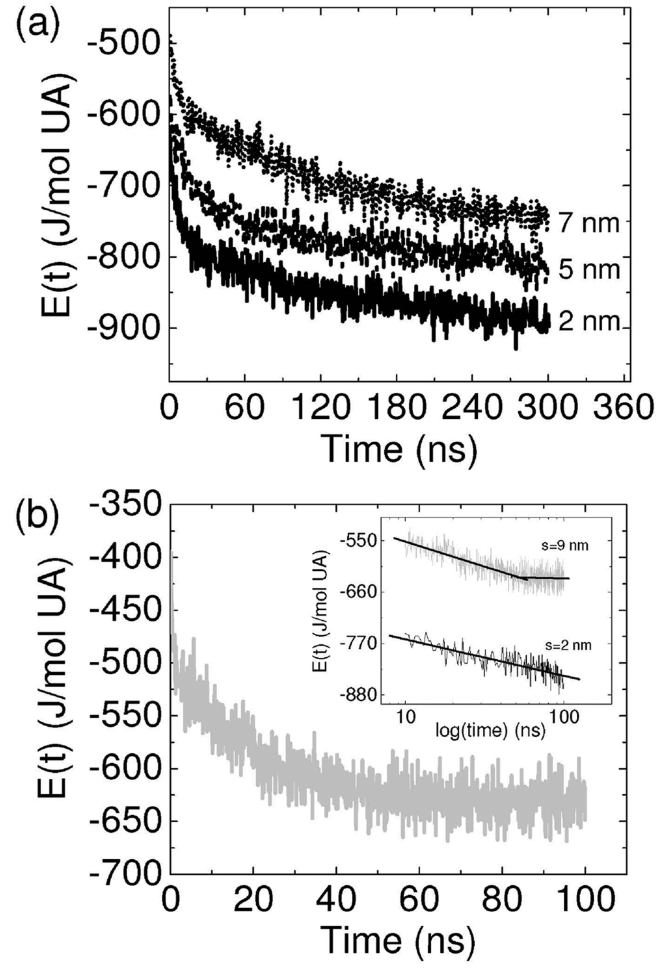

FIGURE 2. MD simulations of system potential energy for fiber−fiber equilibration trajectories at 100 K. (a) Potential energy vs time for separation distances of $s = 2$, 5, and 7 nm indicate an initial fast decay followed by a slower decay that persists for hundreds of ns. (b) Potential energy vs time for $s = 9$ nm indicates attainment of a local energy minimum within 50 ns. The inset indicates the energy decay on a log(time) scale, with piecewise linear regressions indicating that the energy level stabilizes for $s = 9$ nm but not for $s = 2$ nm; $s = 5$ and 7 nm data are omitted for clarity but are consistent with the trends for $s = 2$ nm.

During a typical MD trajectory, the potential energy $E(t)$ initially decreases rapidly due to fast rectification of unfavorable contacts, and then continues to decline more slowly. Once a local equilibrium is attained, $E(t)$ fluctuates around an average, constant value. As Figure 2a shows, the potential energy of the nanofibers at 1 nm $< s <$ 9 nm continued to decrease very slowly over the entire course of the 300 ns

MD simulation. For $s \geq 9$ nm, the systems reached equilibrium within approximately $t \sim 50$ ns, after which potential energy fluctuates less than 12% around an average value of −627 J/mol UA (see Figure 2b inset). The time it takes for an MD simulation of such polymeric systems to equilibrate depends on several factors, including molecular weight and temperature; however, these fiber−fiber simulations were run under identical molecular weight and temperature conditions. The separation distance determines the degree of interaction between the fibers at early times, and can affect the time required for the fiber−fiber system to reach a local energetic minimum (29). Because the fiber radius (as defined by the Gibbs dividing surface) is 2.3 nm, the fibers overlap significantly at $s = 2$, 3, and 4 nm. Furthermore, the surface regions of nanofibers are actually finite in thickness; we have reported previously that the interfacial thickness of these fibers, defined here as the distance over which the mass density of the fiber decreases from 90 to 10% of the bulk value, is 1.4 nm, independent of fiber diameter (26). This thickness of an effective surface "layer" indicates that the density of polymer segments is significant out to a distance from the fiber core of ∼3.0 nm in these fibers. The actual position of individual segments of chains may fluctuate to distances even further than this from the fiber axis because of thermal motion. Because of these fluctuations, fibers can interact even for values of s as large as 8 nm, which presumably accounts for the long and incomplete equilibration times observed here. For $s > 9$ nm, no interaction between the fibers was observed (as defined by molecular overlap between chains from distinct fibers over the simulated trajectories) and the system reached a local energetic minimum, indicated by a stable energy value, within 50 ns.

Radial Density and Cross-Sectional Shape Profiles. We calculated the radial density profiles (details of this calculation can be found elsewhere (26)) of one fiber within our MD simulations at different s, in order to analyze structural changes of the fiber at the molecular level (Figure 3a). The density profile of a single, separately equilibrated fiber is also given in Figure 3a as a reference point, to emphasize the differences in atomic mass density profiles due to interfiber interactions.

In the case of a single, isolated fiber, the density is constant and highest within the core of the fiber and equal to ∼0.9 g/cm^3. In contrast, in the case of two fibers at a separation distance $s = 2$ nm, the region of highest mass density in a single fiber is displaced outward from the fiber core. (However, as will be shown shortly, this displacement is not radially symmetric.) Furthermore, this density is lower than in the case of the isolated fiber, at ∼0.6 g/cm^3; a similar trend is observed at $s = 3$ nm. At $s = 4$ and 5 nm, the mass density profiles are similar to that of an isolated single fiber. The distortion of the density profiles at $s = 2$ and 3 nm are indicative of significant overlap of the two fibers, which necessitates displacement of the chains, on average, away from the COM of each fiber. In other words, the cylindrical symmetry of each fiber is disrupted by this interaction.

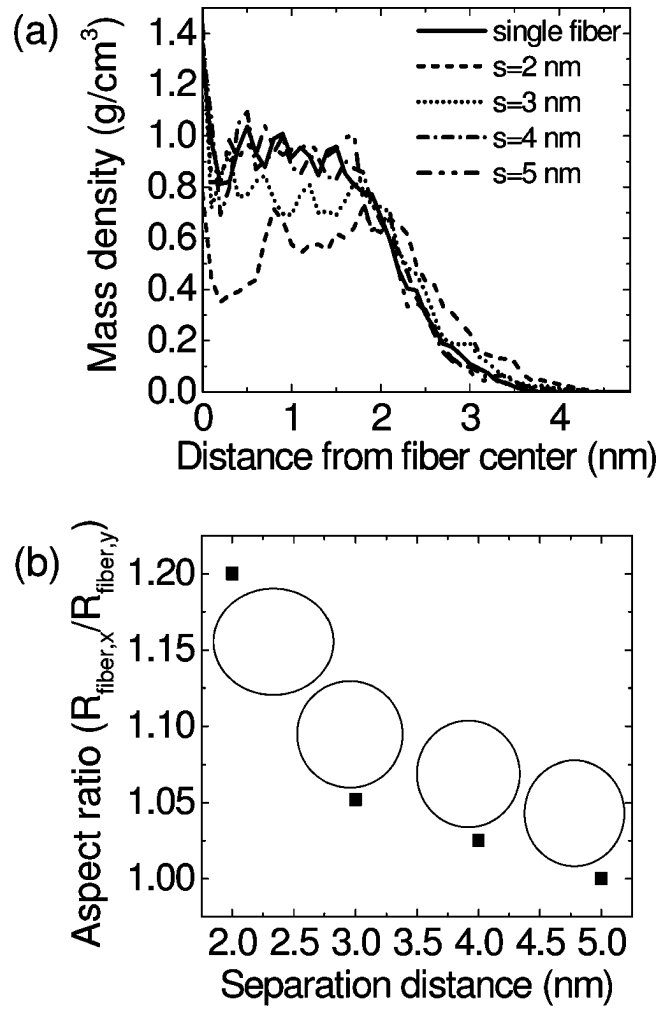

FIGURE 3. (a) Mass density profile of an equilibrated single nanofiber, as compared with the mass density profile of one of the fibers in fiber−fiber MD simulations at different separation distances s. (b) Ellipticity of the fiber cross-section, shown as a function of separation distance for one of the fibers in MD simulations at 100 K, indicates that the cylindrical symmetry is distorted when a second fiber is placed adjacent to an initially cylindrical nanofiber. The drawn ellipses are representative of several cross-sections corresponding to the cross-section ellipticity at each separation distance.

Figure 3b shows the ratio of major and minor axes ($R_{fiber,x}$ and $R_{fiber,y}$, respectively) for the cross-section of one fiber, termed the ellipticity of the fiber cross-section, as a function of separation distance s. Fiber cross-sections become increasingly elliptical for decreasing separation distances. This change in fiber shape is also demonstrated graphically in Figure 3b, where ellipses are drawn to scale to represent the cross-section ellipticity at each separation distance. This ellipticity is the largest (∼1.2) at $s = 2$ nm, where distortion of the mass density profile is greatest.

The changes in both the density and shape profiles suggest that the macromolecular chains tend to intermix from one fiber to another, leading to a constrained coalescence (because s is fixed to be nonzero) of the two fibers. Because the chains are chemically and structurally "identical" in the two fibers, this coalescence can be understood as a consequence of the tendency to reduce the total surface energy of the system, in a manner analogous to particle

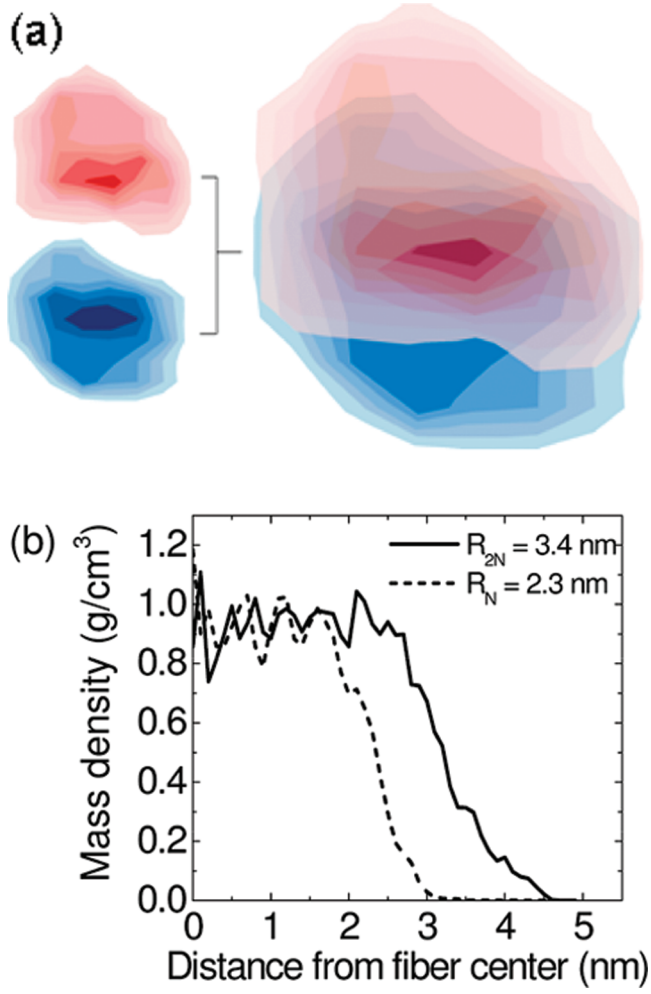

FIGURE 4. (a) Mass density contour plots of fibers within a fiber-pair at s = 2 nm, obtained from time-averaged trajectories over 300 ns of MD simulation for the representative segment length of each fiber. Red and blue shades indicate density within each fiber of the partially coalesced pair, ranging from ~0.9 (dark) in the core to 0.1 (light) at the surface of each fiber. Overlay of these contours (red and blue shaded areas) indicate the state of partial coalescence at 300 ns; (b) the radial mass density profile of a single, isolate fiber (R = 2.3 nm) is compared to that of the larger fiber formed by the partial coalescence of two such nanofibers.

sintering and microstructural coarsening in nonpolymeric materials (30).

The change in cross-sectional profile is also demonstrated in Figure 4a, for a fiber-pair at s = 2 nm and at 300 ns (the maximum extent of coalescence in this MD simulation). For clarity, the mass density contours of each fiber cross-section are indicated separately (shaded either red or blue, and averaged over the length of the representative segment described in Methods), and also in the overlay of these contours (shaded either red or blue) as exists at 300 ns. Figure 4b compares the radial mass density profile of one of the single, isolated nanofibers (R = 2.3 nm) to that of the larger fiber formed by partial coalescence of two such nanofibers. This radial mass density illustrates that the density of macromolecular chains at both the single-fiber and fiber-pair cores are comparable within 300 ns of simulation; however, the distance from the core over which this high density extends is naturally greater for the larger, partially coalesced fiber-pair. Although this coalesced fiber-pair is not cylindrical in cross-section, an estimate of the effective radius obtained by the GDS method is 3.4 nm. This estimate will assist in comparison of the limits of interaction energy in the model discussed below.

At this point, it is worth remarking on the slow decrease in potential energy over a period of 100s of nanoseconds observed in Figure 2a, for cases where $s < 9$ nm. The energy $E(t)$ at any time t is higher for systems with larger s, because the constraint on the separation distance between the fiber COMs implies a final equilibrium configuration that is increasingly distorted from being circular in cross-section, and thus higher in surface energy; only a system in which the constraint on s is completely released, could completely rearrange to form a single, larger fiber. Nevertheless, the magnitude of this decay is remarkable considering the time scale of these simulations, in light of the fact that the temperature of simulation (100 K) was chosen to lie well below not only the glass transition of the core of the fiber (280 K, irrespective of fiber diameter) but also that previously determined to be characteristic of the surface of the fiber (150 K, also irrespective of fiber diameter) (26).

We interpret this energy relaxation as evidence for a small but more mobile fraction of material at the outer periphery of the fibers, which remains highly dynamic even at very low temperature. To quantify the differences between the dynamics of bulk and interfacial regions, we calculated the percentage of united atoms that remained within a given cylindrical shell during the entire MD simulation. This analysis provides a measure of the number of united atoms that had sufficient mobility to move from the fiber core toward the fiber surface (or vice versa), as a function of separation distance between fibers. As shown in Figure 5a, the fibers are divided into concentric cylindrical shells (i.e., bins) of 0.5 nm width, starting from the center or core of the fiber (bin 1, colored blue) toward the free surface of the fiber (bin 6, colored red). As Figure 5b illustrates, only 10−15% of the atoms that initially occupy bin 1 (at the core of the fiber) exit this bin during 300 ns of simulation; this fraction is only weakly dependent on inter-fiber separation distance. In contrast, up to 30% of the united atoms that initially occupy bin 6 (near the surface of the fiber) exit this bin under the same simulation conditions, this fraction being smaller for s = 2 nm than for s = 6 or 9 nm. Thus, the mobility of united atoms near the surface of the fiber decreases significantly when there is appreciable physical overlap between adjacent fibers. In contrast, when the fibers do not overlap appreciably (s = 6 and 9 nm in Figure 5b), the united atom positions fluctuate sufficiently to exit this near-surface region.

Taken together, these data indicate that the degree of mobility of united atoms is greatest at the fiber surface, as compared to the fiber core. This is consistent with our previous studies on these fibers describing an effective T_g in terms of a simplified layer model with a surface region of higher molecular mobility (26). Also, as the bin number increases (from the core toward the surface), the fraction of

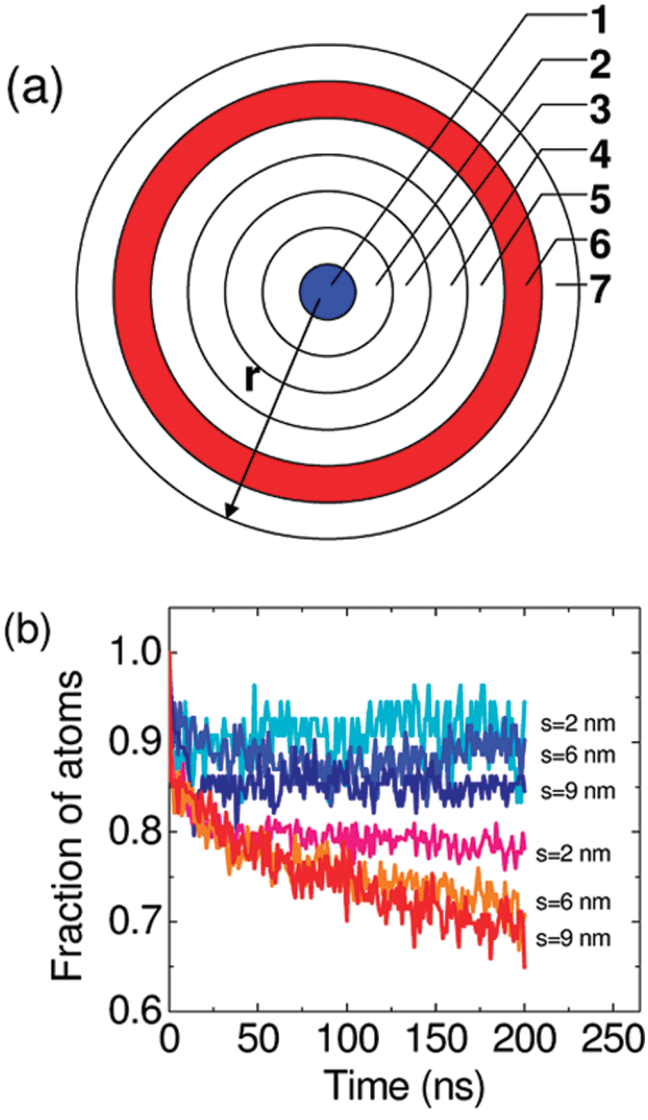

FIGURE 5. Relative mobility of united atoms as a function of distance from the fiber core over time. (a) Circular bins are numbered from 1 to 7, represent the bins; the blue circle at the fiber core represents bin 1; the red circle represents bin 6; (b) fraction of atoms remaining in the same bin they occupied at time zero, as a function of simulation time, for three distinct separation distances *s*. Families of blue lines correspond to $0 < r < 0.5$ nm (bin 1), and families of red lines correspond to $2.5 < r < 3$ nm (bin 6).

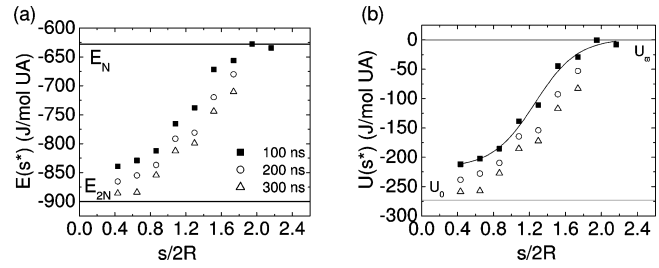

FIGURE 6. (a) Potential energy per mole of united atoms (UA) for the fiber-pair system as a function of s^*, or separation distance s normalized by fiber diameter $2R$. Each data symbol corresponds to the energy $E(t)$ extracted from the simulations at different times: 100 ns (filled squares), 200 ns (open circles), and 300 ns (open triangles). The upper and lower horizontal lines are limits for isolated fibers of radius R_N and R_{2N}, respectively. (b) Interaction energy per mole of UA as a function of s^*, where $E_N(t)$ is subtracted from $E(t)$. Symbols indicate the same time points as in (a). The solid curve illustrates the best fit of the sigmoidal form given by eq 1 to the simulation data at 100 ns; see text for details. Note that equilibration remains incomplete at 300 ns, but the form of the energetic transition with s^* is maintained.

united atoms displaced from the original bin location increases (data not shown). This merely serves as a reminder that the dynamic behavior of the fiber surface varies in a gradient manner as a function of distance from the fiber surface, ranging from that of a low-density fluid at the fiber surface to a glassy solid closer to the fiber core. As the physical dimensions of a material structure (e.g., the diameter of a fiber) are reduced to the nanoscale, the primary effect of a reduction in diameter is to increase the fraction of material with the enhanced mobility of this near-surface region, for both single-fiber properties (26) and the interfiber interactions of interest herein. Note that we have previously found the thickness of this near-surface layer to be independent of fiber radius and dependent on temperature (26). (Even for small systems such as the current fiber-pairs of 4.6 nm fiber diameter, however, complete relaxation of the fiber-pair mediated by this mobile surface fraction is too slow to follow to completion, requiring real simulation times in excess of 3 months on a single 2.66 GHz dual-quad core in LAMMPS; this is beyond the scope of the current study.)

Fiber-Pair Interaction Model. From these MD simulations, we can approximate the interaction between two fibers by comparing the energies of the two-fiber system to that of single, isolated fibers. Note that the rigorous calculation of a potential of mean force between two fibers constrained by the distance s would require the incremental accumulation of differences in free energy, $\Delta G(s)/kT = -\ln\langle\exp[\Delta E(s)/kT]\rangle_s$, over many small increments of s, according to perturbation theory (31); however, given the long equilibration times exhibited by Figure 2, such a calculation becomes computationally prohibitive and is not essential to the conclusions reached in this study. Figure 6a shows the potential energy per mole of united atom (mol UA) as a function of $s^* = s/2R$, the separation distance normalized by the diameter of the fibers, $2R = 4.6$ nm. For any given snapshot of simulation time longer than about 50 ns (the single fiber equilibration time), this potential energy varies smoothly between that of two isolated fibers each of $R = 2.3$ nm (the upper bound marked E_N, where the linear density $N/L = 3000/4.3$ nm, or 1.6×10^{-8} tex in units common to textile science) at large distances and that of an isolated fiber with $R = 3.4$ nm, having twice this linear density (the lower bound marked E_{2N}). With increasing simulation time, these potential energy data shift downward, with little change in the shape of the variation between E_N and E_{2N} (e.g., compare $t = 200$ and 300 ns in Figure 6). To obtain the interaction energy $U(s^*)$, we subtract E_N from the total potential energy of the fiber-pair system at each s^* (Figure 6b).

On the basis of these observations, we construct a mathematical function that describes the interaction $U_{MD}(s^*)$ between two nanofibers as a function of the normalized separation distance $s^* = s/2R$. Such normalization of separation distance enables future considerations of other fiber radii or interaction models, and the energetic subscript MD

indicates macromolecular thermal fluctuations within and between fibers afforded by MD algorithms. The form of the interaction is well-described by the logistic function

$$U_{MD}(s^*) = U_0 + (U_\infty - U_0)\left[1 + \exp\left(-\frac{s^* - s_0^*}{\sigma}\right)\right]^{-1} \quad (1)$$

where s_0^* and σ serve to translate and rescale, respectively, the independent variable s^*, whereas U_0 and $(U_\infty - U_0)$ serve to translate and rescale, respectively, the dependent variable $U_{MD}(s^*)$. Here, energy tends to U_0 as s^* tends to 0 (full coalescence) and to U_∞ as s^* goes to $+\infty$ (distant, isolated fibers). The inflection point of this interaction energy is located at s_0^*, whereas σ gives a sense of the strength of this dependence and is sometimes referred to as the "steepness parameter". The form of this function predicts that within a certain (small) distance of approach, two fibers experience an attractive force driving them into contact, with a work of adhesion on the order of $(U_\infty - U_0)$. Here we do not report fitted parameters of our MD simulation data to predict $U_{MD}(s^*)$ in closed form, as Figure 6b makes clear that this system has not yet attained the equilibrium state this function aims to describe; that state would span the physical limits U_0 and U_∞ over these simulation length scales. However, reasonable order-of-magnitude estimates of such fitting parameters for this specific system can be obtained readily from Figure 6b, and the general form of $U_{MD}(s^*)$ is expected to be generally applicable to interactions between fibers of other nanoscale radii, provided the assumptions of this modeling perspective apply.

Note that these limiting energetic values U_0 and U_∞ are not arbitrary results of fits to MD simulations of fiber-pairs, but in fact can be related directly to the surface energy. We have previously shown that the energy of an isolated fiber, even at such small diameters, is well-described by the following equation

$$E_N = E_{bulk} + \gamma(2\pi R_N L)N_A/N \quad (2)$$

where N_A is Avogadro's number, N/L is the number of UA per unit length L of fiber, R_N is the radius of the fiber (here, 2.3 nm), E_{bulk} is the molar energy density of UA in the bulk amorphous phase (1.67 J/mol UA or 102 J/cm^3 at 100 K), and γ is the surface energy (~45 mJ/m^2 (26)), which we have found to be independent of nanoscale fiber radius. This surface energy is also in agreement with an experimental estimate of 44.7 mJ/m^2 for amorphous PE at 100 K (32). When two fibers of radius R_N coalesce completely to form a single, larger fiber of radius R_{2N} (here, 3.4 nm), the change in energy is predicted by continuum thermodynamic analysis to be

$$\Delta E = E_{2N} - E_N = \frac{\pi L N_A \gamma}{N}(R_{2N} - 2R_N) \quad (3)$$

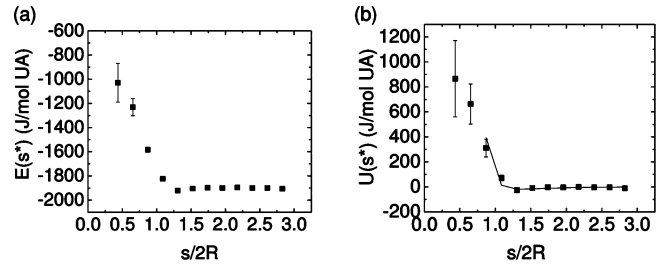

FIGURE 7. (a) Total potential energy as a function of separation distance $E(s^*)$ calculated from molecular statics (MS). (b) Net interaction energy as a function of separation distance $U_{MS}(s^*)$, obtained by subtracting the energy for two noninteracting fibers, E_∞, from $E(s^*)$ (see text for details). Data points represent the MS calculation results, and the solid line is the best fit to the MS calculation data using eq 4.

We compute this energy difference to be $\Delta E = -290$ J/mol UA, using the above values for N/L, γ, R_{2N} and R_N, which is similar in magnitude to the anticipated work of adhesion given by Figure 6b, $(U_\infty - U_0) = 273$ J/mol UA. Thus, the work of adhesion for interfiber contacts by this approach is consistent with the change in energy due to a reduction in total surface area of a fiber-pair.

Interfiber Interaction Potential Constructed from MS Calculations. We also used a conjugate gradient method (33) to perform energy minimizations or molecular statics (MS) calculations of the same fiber-pair systems as those discussed above for MD simulations (see Methods). Figure 7a shows the potential energy as a function of s, averaged over an ensemble of 36 systems at each s^*. For all separation distances $s \geq 7$ nm, the potential energy is approximately equal to the total energy of two noninteracting fibers, and can be taken as E_∞ for this set of calculations. Subtracting E_∞ from the total potential energy of these MS calculations, we obtain the interfiber interaction energy $U_{MS}(s^*)$ shown in Figure 7b. At $s = 6$ nm, there is an attractive energy well depth of approximately 26.5 J/mol UA; for $s < 6$ nm, the force of interaction between these fibers is repulsive, in direct contrast to the results obtained for these fibers via MD simulations. Interestingly, $s = 6$ nm corresponds to a separation distance slightly larger than s^*_0 (see eq 1), where the density of polymer segments is still significant. The range of attractive interaction is narrow (extending ~1 nm), indicating a short-range attraction between these nanoscale fibers.

In contrast to the MD simulations of fiber pairs, the interfiber interaction energy as a function of separation distance obtained by MS is reminiscent of classical pair potentials between particles. We found best agreement between our MS-calculated $U_{MS}(s^*)$ and an interaction potential of the Mie form, with $(m,n) = (8,4)$:

$$U_{MS}(s^*) = A(s^*)^{-8} - B(s^*)^{-4} \quad (4)$$

Again, s^* is the normalized separation distance $s/2R$ and the energetic subscript MS indicates energetic states attained under molecularly static interactions within and between chains of the interacting fibers. As Figure 7b shows, eq 4 can success-

fully predict the interaction energy $U_{MS}(s^*)$ of such fiber pairs for $s > 3$ nm. At $s = 2$ and 3 nm (i.e., $s/2R < 0.7$), this model overpredicts the repulsive energy by 2 orders of magnitude, and thus is not shown in Figure 7b. (Many variations of the Mie potential, as well as other forms such as piecewise exponential decays, were considered; however, none of those other forms were any better in capturing both the trends at small s and the depth and curvature of the energy minimum at $s \sim 6$ nm.) The form of eq 4 thus summarizes the interaction potential between two fibers up to the point at which the fiber radii defined by the GDS begin to intersect (here, for $s < 4$ nm). Physically, this corresponds to separation distances of significant overlap between the chains in adjacent nanofibers that extend beyond the GDS.

Note that the energies from MD and MS calculations change in a different manner as a function of separation distance, resulting in different forms of the interfiber interaction potential (eqs 1 and 4, respectively). There is both a simulation-specific rationale and a physical parallel for these differing perspectives, which is discussed in the next section.

Relation of Modeling Perspectives to Physical Conditions. Both MD simulations and MS calculations indicate that there exists a short-ranged attractive interaction between fibers that extend out to a distance s of $3R_{fiber}$ to $4R_{fiber}$ (for $R_{fiber} = 2.3$ nm). However, whereas MD simulations predict an eventual coalescence of the nanofibers with a significant work of cohesion, MS calculations predict that the interaction between fibers becomes repulsive for smaller separation distances. As discussed in Methods, for a given constraint such as fixed separation distance between fiber COMs, the MS approach affords limited atomic reconfigurations to attain a local energetic minimum (hence, "molecular statics" governing $U_{MS}(s^*)$). This is in contrast to the MD approach that allows greater exploration of macromolecular configuration space via thermal fluctuations at a prescribed temperature (hence, "molecular dynamics" governing $U_{MD}(s^*)$). To consider the relevant time scales of interest for these fibers, one can compare various measures of relaxation times in glassy solids and low-density melts. Yin and Boyd have previously estimated that the time scale of the γ relaxation below T_g for a UA model of this polymer (of chain length C768) in the bulk state is on the order of 32 μs (34), which is far longer than our MD simulations here. However, the enhanced mobility of PE-like chains near the surface may permit much faster relaxation; estimates of the Rouse time for a UA model of C100 above its T_g are on the order of 2.5 ns (35), which is well within the time scale of these MD simulations.

To identify the situations involving electrospun polymeric fibers for which $U_{MD}(s^*)$ and $U_{MS}(s^*)$ may be most appropriate, we consider the relation between the relevant material relaxation time and the laboratory time scale. For example, if the fibers are in contact with each other and the chains near the surfaces are sufficiently mobile (analogous to the MD simulation perspective), the fibers tend to coalesce. This prediction correlates with experimental observations of interfiber "welding" when electrospun nonwoven materials are laid down "wet", or are annealed at high temperatures (10) or in the presence of a plasticizing agent or solvent (11−13). The role of temperature or solvent in this case is to decrease the relevant material relaxation time, or to increase the fraction of macromolecular chains with elevated mobility at the fiber surfaces, such that a significant reconfiguration and subsequent consolidation of the fibers at the point of contact can be achieved (7−10). In contrast, if the contacts between fibers are strictly "solid-like" and very limited macromolecular reconfigurations are permitted (analogous to the MS calculation perspective), the fibers interact repulsively when the fibers overlap significantly and exhibit a weak, short-ranged interfiber attraction when they do not overlap. Naturally, this repulsion arises from the elevated mass density of the overlapping fibers, but is a softer repulsion than would be suggested by a rigid-cylinder solid. This situation correlates with the more conventional case of cooled (or quenched) fibers interactions in the post-electrospun state at temperatures far below the bulk glass transition temperature of the polymer. As the diameter of fibers in contact is reduced, the relative contribution of this mobile surface fraction and its attendant shorter time scale of relaxation, become more important to the overall properties of the single fibers and to the interfiber interactions. Thus, one anticipates that a transition from the solid-like contact picture to the dynamic, cohesive contact picture may be observed for sufficiently small diameter fibers at constant system temperature.

As a final caveat, we reiterate that the results discussed herein pertain to simulations for a single fiber-diameter of 4.6 nm, wherein fibers of infinite length are aligned in parallel. Interfiber potentials are presented as a function of scaled separation distance, $s^* = s/2R$ (eqs 1 and 4 and Figures 6 and 7). Given the radius-independent thickness and molecular mobility of the near-surface layer of these amorphous fibers (26), we anticipate (but have not shown) that this scaling may also hold for fibers of other radii. Further, fibers of finite length are not explicitly considered, such that end effects are neglected and local elastic instabilities within and between the interacting fibers are not observed and thus do not contribute to the predicted $U(s^*)$. Although the fiber radii and simulation times herein are necessarily small compared to most current electrospun fibers and experimentally accessible time scales, respectively, the present findings and predictions may motivate further studies to explore the size-dependent nature of interfiber interactions in nonwoven materials.

CONCLUSIONS

Previous studies of nonwoven materials modeling (14−19) have employed several different forms of interfiber interactions, without any strong justification for these forms at the molecular level. Here we have studied the interfiber interactions by two distinct atomistic simulation methods, in order to develop a quantitative understanding and prediction of interfiber interaction energies. We propose two interfiber potentials constructed directly from atomistic simulations of individual nanofiber pairs. The resulting

formulas capture trends from MD simulations (eq 1) and MS calculations (eq 4) for nanoscale polymer fibers. Both perspectives find reasonable analogy with different, specific experimental conditions that have been realized for electrospun polymer nanofiber-based materials, and point toward future experiments and models that will test and exploit these interactions. These interfiber effective potential models serve as a useful starting point to represent accurately the interactions between fibers in nonwoven material models. Further, the comparison between these approaches suggests the need for new experiments and models to explore the critical length scales and time scales of interfiber interactions in polymeric systems at the nanoscale.

Acknowledgment. This work was funded in part by the DuPont-MIT Alliance (G.C.R. and S.C.B.) and the Thomas Lord Foundation Chair and NSF CAREER Awards (to K.J.V.V.).

REFERENCES AND NOTES

(1) Barhate, R. S.; Ramakrishna, S. *J. Membr. Sci.* **2007**, *296*, 1.
(2) Martins, A.; Araujo, J. V.; Reis, R. L.; Neves, N. M. *Nanomedicine* **2007**, *2*, 929.
(3) Liang, D.; Hsiao, B.; Chu, B. *Adv. Drug Delivery Rev.* **2007**, *59*, 1392.
(4) Yeo, L. Y.; Friend, J. R. *J. Exp. Nanosci.* **2006**, *1*, 177–209.
(5) Burger, C.; Hsiao, B.; Chu, B. *Ann. Rev. Mater. Res.* **2006**, *36*, 333.
(6) Zong, X.; Ran, S.; Fang., D.; Hsiao, B. S.; Chu, B. *Polymer* **2003**, *44*, 4959.
(7) Choi, S. S.; Lee, S. G.; Joo, C. W.; Im, S. S.; Kim, S. H. *J. Mater. Sci.* **2004**, *39*, 1511.
(8) Young, Y.; Lee, S. W.; Lee, S. J.; Park, W. H. *Mater. Lett.* **2006**, *60*, 1331.
(9) Lee, S. J.; Oh, S. H.; Liu, J.; Soker, S.; Atala, A.; Yoo, J. J. *Biomaterials* **2008**, *39*, 1422.
(10) Choi, S.; Lee, S. G.; Joo, C. W.; Im, S. S.; Kim, S. H. *J. Mater. Sci.* **2004**, *39*, 1511.
(11) Lee, K. H.; Kim, H. Y.; La, Y. M.; Lee, D. R.; Sung, N. H. *J Polym. Sci. Polym. Phys.* **2002**, *40*, 2259.
(12) Krishnappa, R. V. N.; Desai, K.; Sung, C. *J. Mater. Sci.* **2003**, *38*, 2357.
(13) Kidoaki, S.; Kwon, K.; Matsuda, T. *J. Biomed. Mater. Res., Part B: Appl. Biomater.* **2005**, *76B*, 219.
(14) Pan, N.; Carnaby, G. A. *Text. Res. J.* **1989**, *59*, 285.
(15) Komori, T.; Itoh, M. *Text. Res. J.* **1991**, *61*, 420.
(16) Narter, M. A.; Batra, S. K.; Buchanan, D. R. *Proc. R. Soc., A* **1999**, *455*, 3543.
(17) Wang, C. W.; Berhan, L.; Sastry, A. M. *J. Eng. Mater. Technol.* **2000**, *122*, 450.
(18) Astrom, J. A.; Makinen, J. P.; Alava, M. J.; Timonen, J. *Phys. Rev. E* **2000**, *61*, 5550.
(19) Wu, X. F.; Dzenis, Y. A. *J. Appl. Phys.* **2005**, *98* (1−9), 093501.
(20) Chatterjee, A. P. *J. Appl. Phys.* **2006**, *100* (1−8), 054302.
(21) Wu, X.; Dzenis, Y. A. *J. Phys. D* **2007**, *40*, 4276.
(22) Plimpton, S. *J. Comput. Phys.* **1995**, *117*, 1.
(23) Paul, W.; Yoon, D. Y.; Smith, G. D. *J. Chem. Phys.* **1995**, *103*, 1702.
(24) Bolton, K.; Bosio, S. B. M.; Hase, W. L.; Schneider, W. F.; Hass, K. C. *J. Chem. Phys. B* **1999**, *103*, 3885.
(25) In't Veld, P. J.; Rutledge, G. C. *Macromolecules* **2003**, *36*, 7358.
(26) Curgul, S.; Van Vliet, K. J.; Rutledge, G. C. *Macromolecules* **2007**, *40*, 8483.
(27) Buell, S.; Van Vliet, K. J.; Rutledge, G. C. *Macromolecules* **2009**, *42*, 4887.
(28) Capaldi, F. M.; Boyce, M. C.; Rutledge, G. C. *Polymer* **2004**, *45*, 1391.
(29) Walton, E. B.; Van Vliet, K. J. *Phys. Rev. E* **2006**, *74* (1−8), 061901.
(30) Pan, J. Z. *Int. Mater. Rev.* **2003**, *48*, 69.
(31) Linse, P. *J. Am. Chem. Soc.* **1993**, *115*, 8793.
(32) Brandup, J.; Immergut, E. H.; Grulke, E. A.; Abe, A.; Bloch, D. R. In *Polymer Handbook*, 4th ed.; John Wiley & Sons: New York, 1999.
(33) Nocedal, J.; Wright, S. J. In *Numerical Optimization*, 2nd ed.; Springer-Verlag: New York, 2006.
(34) Jin, Y.; Boyd, R. H. *J. Chem. Phys.* **1998**, *108*, 9912.
(35) Harmandaris, V. A.; Mavrantzas, V. G.; Theodorou, D. N. *Macromolecules* **1998**, *31*, 7934.

AM1000135